Check for updates

A comparison study of MnO$_2$ and Mn$_2$O$_3$ as zinc-ion battery cathodes: an experimental and computational investigation†

Hongyuan Shen, [ID] ‡*[a] Binbin Liu,‡[b] Zanxiang Nie,[c] Zixuan Li,[b] Shunyu Jin,[d] Yuan Huang[e] and Hang Zhou [ID] [b]

The high specific capacity, low cost and environmental friendliness make manganese dioxide materials promising cathode materials for zinc-ion batteries (ZIBs). In order to understand the difference between the electrochemical behavior of manganese dioxide materials with different valence states, *i.e.*, Mn(III) and Mn(IV), we investigated and compared the electrochemical properties of pure MnO$_2$ and Mn$_2$O$_3$ as ZIB cathodes *via* a combined experimental and computational approach. The MnO$_2$ electrode showed a higher discharging capacity (270.4 mA h g^{-1} at 0.1 A g^{-1}) and a superior rate performance (125.7 mA h g^{-1} at 3 A g^{-1}) than the Mn$_2$O$_3$ electrode (188.2 mA h g^{-1} at 0.1 A g^{-1} and 87 mA h g^{-1} at 3 A g^{-1}, respectively). The superior performance of the MnO$_2$ electrode was ascribed to its higher specific surface area, higher electronic conductivity and lower diffusion barrier of Zn^{2+} compared to the Mn$_2$O$_3$ electrode. This study provides a detailed picture of the diversity of manganese dioxide electrodes as ZIB cathodes.

1. Introduction

In recent years, zinc-ion batteries (ZIBs) have received significant attention because Zn is naturally abundant, and ZIB devices, which are based on an aqueous electrolyte, are safer and more environmentally friendly compared to lithium-ion batteries.[1–4] Manganese dioxide materials are considered as promising candidates for cathode materials for ZIBs.[5–14] This is due to their high specific capacity, low cost, and environmental friendliness.[3] The studies available on manganese dioxide cathodes for ZIBs mainly focus on MnO$_2$,[15–18] Mn$_2$O$_3$,[19] Mn$_3$O$_4$ (ref. 9 and 20) or mixed-valence manganese dioxide containing multiple phases.[3,21] For instance, Fu *et al.* synthesized porous MnO$_x$ (Mn(IV) and Mn(II)) nanorods with N-doped carbon by the metal–organic framework method as a new cathode for ZIBs.[21] These ZIBs delivered a relatively high specific capacity of

[a]College of Information Science and Engineering, Northeastern University, Shenyang, PR China. E-mail: shenhongyuan@ise.neu.edu.cn

[b]School of Electronic and Computer Engineering, Peking University Shenzhen Graduate School, Shenzhen, 518055, PR China

[c]Zinergy Shenzhen Ltd., Floor 6, Building H, Gangzhilong Science Park, Longhua, Shenzhen, 518109, PR China

[d]Center for Micro- and Nanoscale Research and Fabrication, University of Science and Technology of China, Hefei, 23000, PR China

[e]School of Microelectronics Science and Technology, Sun Yat-Sen University, Guangzhou, PR China

† Electronic supplementary information (ESI) available. See DOI: 10.1039/d1ra00346a

‡ These authors contributed equally to this work.

385 mA h g^{-1} after 120 cycles. The composite cathodes showed excellent rate performance and good cycle retention.

In our previous study, we utilized MnO$_x$/polypyrrole (PPy) composites containing Mn(III) and Mn(IV) phases as Zn intercalation host cathodes in aqueous ZIBs.[3] The electrochemical properties of the MnO$_x$/PPy electrode were fairly sensitive to the amount of manganese dioxides phases, *i.e.*, Mn(III) and Mn(IV). This inspired us to explore the difference between the electrochemical performance of manganese dioxides with Mn(III) phase and Mn(IV) phase as well as the contribution of the different phases to the electrochemical properties of the mixed-valence MnO$_x$ electrode. However, the mixed-valence MnO$_x$ electrode is composited with other additives (*i.e.*, PPy), and possible contributions from multiple factors make it difficult to identify the role of each phase. In addition, a few factors (*e.g.*, the diffusion barrier of Zn^{2+}) that cannot be directly confirmed by experimental means are often ignored, leading to an incomplete analysis. It has been reported that density functional theory (DFT) can be used to simulate the diffusion barrier of Zn^{2+} in cathode materials. Thus, in order to understand and reveal the underlying mechanisms, it is necessary to adopt the related computational methods, and combine the theoretical predictions with the experimental results.

In this study, we investigated and compared the electrochemical properties of pure MnO$_2$ and Mn$_2$O$_3$ as ZIB cathodes *via* a combined experimental and computational study. While manganese dioxides containing Mn(III) and Mn(IV) phases in mixed-valence MnO$_x$ are often more complex than those presented in this study, an understanding of the basic behavior of

the component materials can be helpful in interpreting the behavior of related systems. This study, in combination with our previous work on MnO_x/PPy composites containing Mn(III) and Mn(IV) phases, provides a detailed picture of the diversity of manganese dioxide electrodes.

2. Experimental

2.1 Preparation of MnO_2 and Mn_2O_3 cathode

The α-MnO_2 powder was prepared by a hydrothermal method.[22] 0.1264 g of potassium permanganate, 0.0428 g of $(NH_4)_2SO_4$, and 40 mL of distilled water were added to a Teflon-lined reactor and mixed, and then, treated hydrothermally at 140 °C for 24 h. Then, the resulting powder was filtered by an aqueous filter paper (JINTENG, with a pore size of 200 nm), and washed using distilled water, and dried at 70 °C for 4 h. The as-obtained α-MnO_2 powder was then annealed at 300 °C for 1 h.

The α-Mn_2O_3 powder (CAS No. 1317-34-6) was purchased from Xiya Chemical Industry Company. Super P (conductive additive), with the size of ~40 nm, was purchased from TIMCAL from Switzerland.

To prepare the MnO_2 cathode, 70 wt% of MnO_2 powder, 20 wt% of Super P, and 10 wt% of polyvinylidene fluoride (PVDF) was dispersed in N-methyl-pyrrolidone (NMP), and stirred for 4 h. Then, the mixed slurry was coated onto a carbon cloth and dried at 70 °C for 6 h. The Mn_2O_3 cathode was prepared by the same process. The mass loading of the active mass (MnO_2 or Mn_2O_3) was ~2 mg cm^{-2}, and the geometrical electrode area was ~1.54 cm^2.

2.2 Material characterization

Scanning electron microscopy (SEM, ZEISS SUPRA, Carl Zeiss) was performed to observe the surface morphology of the materials. X-ray powder diffraction (XRD) patterns were recorded using a Bruker X-ray diffractometer (D8 Advance). Nitrogen adsorption/desorption isotherms and pore-size distributions were collected with an accelerated surface-area and porosimetry system (ASAP 2020 HD88).

2.3 Electrochemical characterization

A full battery was assembled from a cathode (MnO_2 or Mn_2O_3), an anode (Zn foil) and a separator (NKK separator) in a solution of 2 M $ZnSO_4$ + 0.1 M $MnSO_4$. The cyclic voltammetry (CV) and electrochemical impedance spectroscopy (EIS) were conducted on an electrochemical workstation (CHI 660e, Shanghai CH Instrument Co., Ltd.) using the full batteries. The CV spectra were recorded within a potential range of 1.0 to 1.9 V vs. Zn/Zn^{2+} at a scan rate at 0.5 mV s^{-1}. The EIS spectra were recorded in a frequency range from 0.01 to 10^5 Hz after charging to ~1.9 V vs. Zn^{2+}/Zn. The galvanostatic charge/discharge tests were conducted in a potential range from 1.0 to 1.9 V vs. Zn/Zn^{2+} using a Land test system (CT2001A, Wuhan Land Electronic Co., Ltd.).

2.4 Computational method and models

All calculations were carried out using the projector augmented wave method in the framework of the DFT,[23] as implemented in the Cambridge Serial Total Energy Package (CASTEP).[24] The generalized gradient approximation (GGA) and Perdew–Burke–Ernzerhof (PBE) exchange functional[23] were used. The plane-wave energy cutoff was set to 500 eV, and the Monkhorst–Pack method[25] was employed for the Brillouin zone sampling. The Monkhorst–Pack method with $3 \times 3 \times 3$ and $3 \times 3 \times 5$ k-point meshes were employed for the Brillouin zone sampling of the α-Mn_2O_3 unit cell and α-MnO_2 $1 \times 1 \times 2$ supercell. The convergence criteria of energy and force calculations were set to 10^{-5} eV per atom and 0.01 eV Å^{-1}, respectively. The Zn-inserted α-MnO_2 structure was built as a $1 \times 1 \times 2$ supercell with a Zn atom at the hollow site.[26] For Mn_2O_3, two different types of adjacent interstitial sites were considered for Zn insertion, namely the tetrahedral and octahedral sites. The linear synchronous transition and quadratic synchronous transition methods[27] implemented in the CASTEP were used to calculate the energy landscape and activation energy barrier of the Zn diffusion in α-MnO_2 and Mn_2O_3.

3. Results and discussion

The crystal structures and morphologies of the MnO_2 and Mn_2O_3 powders were measured by XRD and SEM. The XRD characterization, as shown in Fig. 1(a) and (b), shows that the Bragg peaks can be indexed to the crystalline phases of α-MnO_2 (JCPDS: 44-0141) in Fig. 1(a) and α-Mn_2O_3 (JCPDS: 41-1442) in Fig. 1(b). The morphology of the α-MnO_2 powder, as shown in Fig. 1(c), can be described as nanosheets with lengths and width in the micrometer scale and thickness in less than tens of nanometers. On the other hand, the morphology of α-Mn_2O_3, as shown in the SEM image in Fig. 1(d), consisted of nanoparticles of size in the range of hundreds of nanometers.

The specific surface area and the pore size distribution of the electrode materials play an important role in ion transport, which has been confirmed by previous studies on batteries.[4] Herein, the microporous structure of the MnO_2 and Mn_2O_3 electrodes was confirmed by N_2 adsorption–desorption isotherms and was found to be a typical type-IV isotherm (Fig. 2). The specific surface area of the MnO_2 electrode (61.9 m^2 g^{-1}) was much greater than that of the Mn_2O_3 electrode (10.6 m^2 g^{-1}), resulting in faster ion diffusion between the electrolyte and MnO_2. It is worth noting that the pore diameter distribution of the MnO_2 electrode was mainly located between 1 and 7 nm, and the pore volume was 0.44 cm^3 g^{-1}. Comparatively, the pore diameter distribution of the Mn_2O_3 electrode lay mainly in the range of 20–50 nm, and the pore volume was 0.14 cm^3 g^{-1}. Large numbers of micropores provided more sites for Zn^{2+} storage, and an appropriate pore size distribution could improve the transport of Zn^{2+}, resulting in a high-rate performance.

In order to compare the electrochemical performance of the MnO_2 and Mn_2O_3 electrodes, Zn–MnO_2 and Zn–Mn_2O_3 batteries were assembled with a Zn foil anode in an aqueous electrolyte containing 2 M $ZnSO_4$ and 0.1 M $MnSO_4$. Fig. 3(a) shows the cyclic voltammogram of the Zn–MnO_2 and Zn–Mn_2O_3 batteries at a scan rate of 0.5 mV s^{-1} in the voltage range of 1.0–1.9 V vs. Zn^{2+}/Zn. For the Mn_2O_3 cathode, two separate
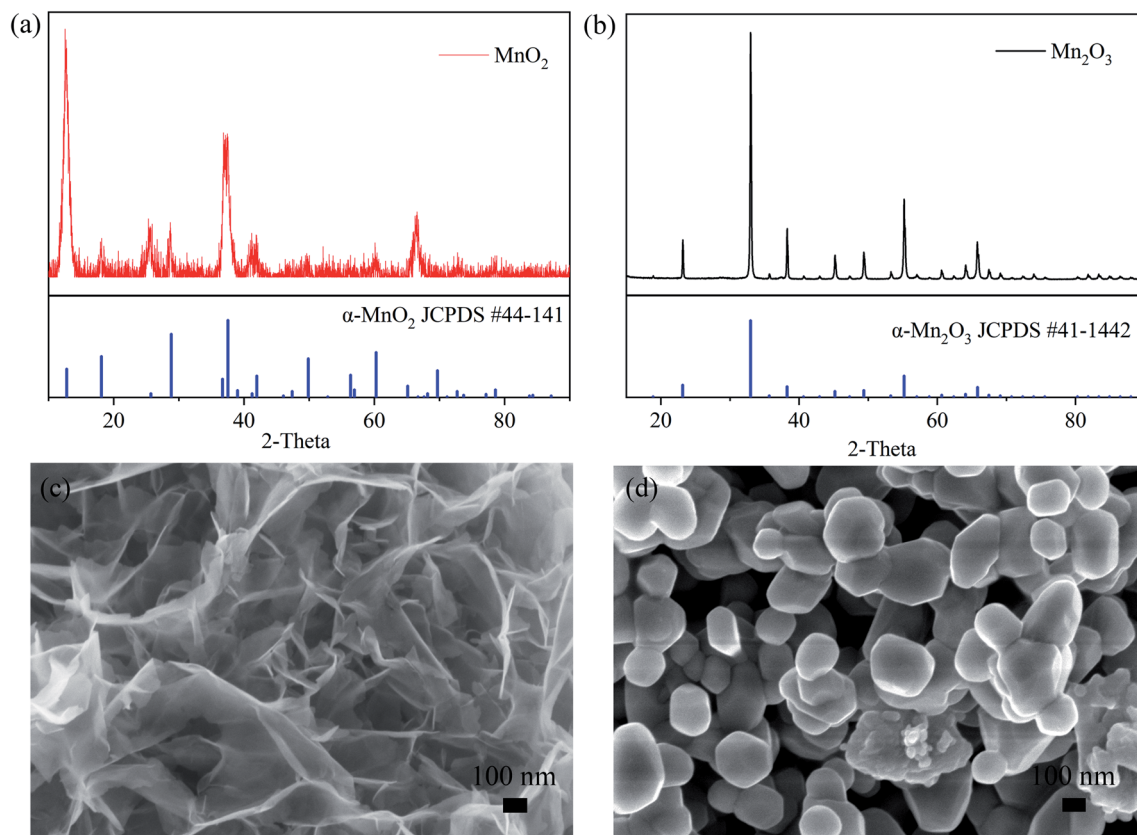
Fig. 1 XRD patterns of (a) MnO_2 and (b) Mn_2O_3. SEM images of (c) MnO_2 and (d) Mn_2O_3.

reversible redox peaks, *i.e.*, reduction peaks at 1.20 and 1.32 V, and oxidation peaks at 1.63 and 1.66 V, were observed, corresponding to a two-step reaction. In comparison, the CV curve of the MnO_2 cathode showed that two similar reduction peaks occurred, while the oxidation peaks merged into a broad peak at 1.62 V. It is worth noting that the Mn_2O_3 electrode showed much lower peaks than those of the MnO_2 electrode, indicating that the Mn_2O_3 electrode had a lower capacity than the MnO_2 electrode.

Fig. 3(b) shows the first, third, and fifth charging and discharging profiles of the MnO_2 and Mn_2O_3 electrodes at a low current density of 0.1 A g^{-1}. In the first cycle, the Mn_2O_3 electrode delivered a low discharge capacity of 61.1 mA h g^{-1}. The capacities at the third and fifth cycles increased to 173.5 and 188.2 mA h g^{-1}, respectively. The increased capacity of the Mn_2O_3 electrode at 0.1 A g^{-1} can be assigned to the gradual activation of electrodes. In comparison, the MnO_2 electrode showed higher and more stable capacities at the first, third, and fifth cycles. The capacities of the MnO_2 electrode at the first,
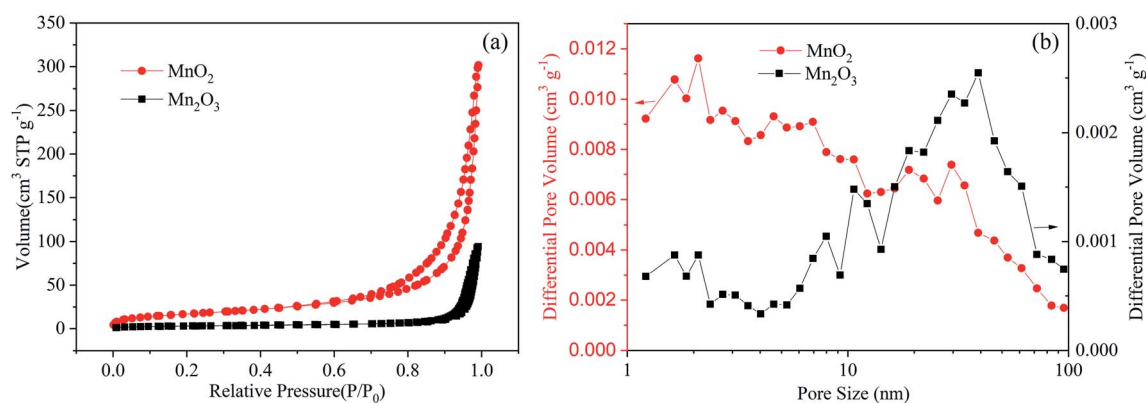

Fig. 2 (a) Nitrogen adsorption/desorption isotherms of the MnO_2 and Mn_2O_3 electrodes. (b) Pore size distributions of the MnO_2 and Mn_2O_3 electrodes.
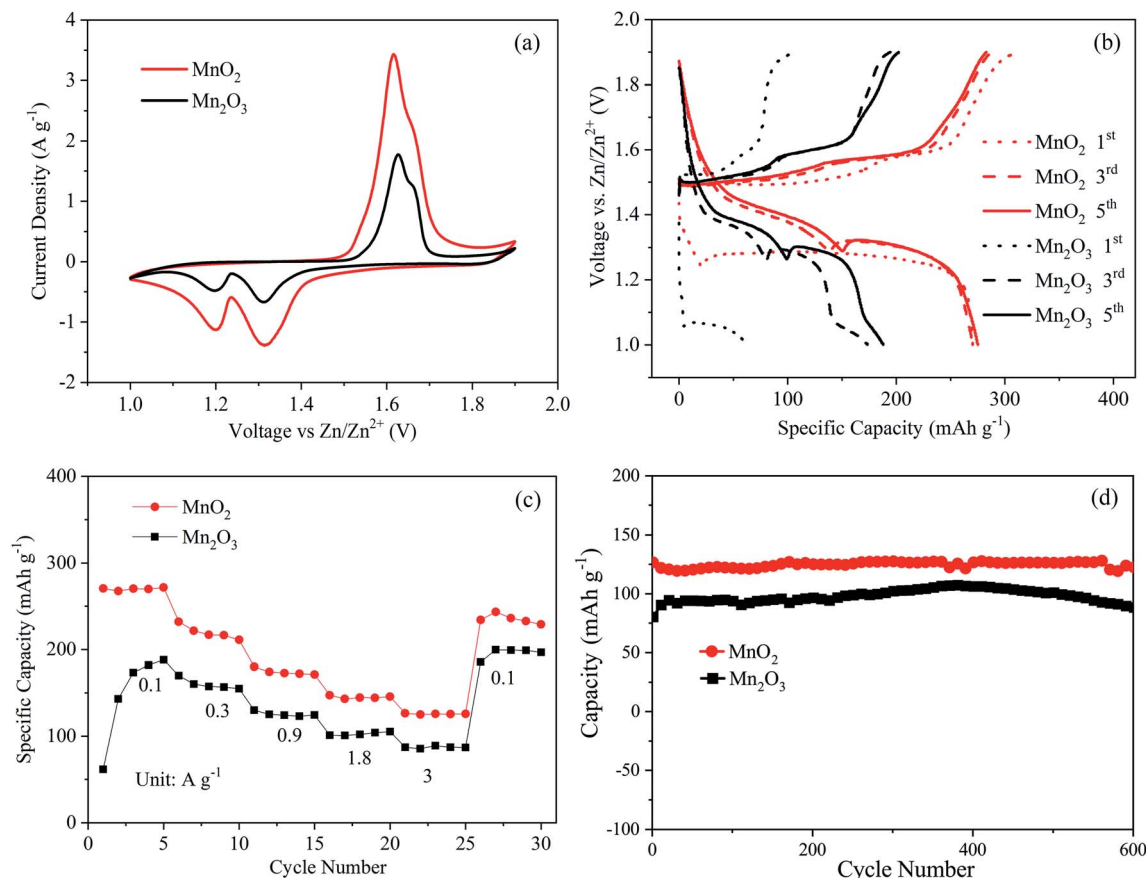
Paper

View Article Online

RSC Advances

Open Access Article. Published on 19 April 2021. Downloaded on 2/5/2026 12:18:30 PM.
This article is licensed under a Creative Commons Attribution-NonCommercial 3.0 Unported Licence.

Fig. 3 (a) Cyclic voltammetry curves of Zn–MnO$_2$ and Zn–Mn$_2$O$_3$ batteries. (b) Discharge/charge profiles of Zn–MnO$_2$ and Zn–Mn$_2$O$_3$ batteries at 0.1 A g^{-1}. (c) Rate capabilities of Zn–MnO$_2$ and Zn–Mn$_2$O$_3$ batteries. (d) Long-term cycling performances of the Zn–MnO$_2$ and Zn–Mn$_2$O$_3$ batteries at 3 A g^{-1}.

third, and fifth cycles were 270.6, 270.4, and 271.7 mA h g^{-1}, respectively. Both electrodes presented similar discharge plateaus, which can be attributed to the consequent H$^+$ and Zn^{2+} insertion processes.[28]

Fig. 3(c) shows the comparison of the rate performance of the MnO$_2$ and Mn$_2$O$_3$ electrodes. Again, the MnO$_2$ electrode exhibited a better rate capability than the Mn$_2$O$_3$ electrode. For instance, the MnO$_2$ electrode could deliver a discharge capacity of 270.4 mA h g^{-1} at a low current density of 0.1 A g^{-1}. When the discharge current density increased to higher values, such as 1.8 and 3.0 A g^{-1}, the discharge capacities were maintained at ~144.6 and ~125.7 mA h g^{-1}, respectively. In comparison, the Mn$_2$O$_3$ electrode exhibited a much lower discharging capacity, i.e., ~102.0 mA h g^{-1} at 1.8 A g^{-1} and ~87 mA h g^{-1} at 3.0 A g^{-1}. The cycling performances of the MnO$_2$ and Mn$_2$O$_3$ electrodes are presented in Fig. 3(d). The MnO$_2$ and Mn$_2$O$_3$ electrodes showed around 96% and 93% capacity retention after 600 cycles, respectively, indicating their excellent cycling performance.

To obtain a better understanding of the difference between the MnO$_2$ and Mn$_2$O$_3$ electrodes, electrochemical impedance spectroscopy (EIS) measurements were carried out after charging to ~1.9 V vs. Zn^{2+}/Zn. The Nyquist plots are shown in Fig. 4. An appropriate equivalent circuit model (inset in Fig. 4)

was established to fit the Nyquist curves. The electrical parameters in this model, namely the ohmic series resistance (R_s), the surface film resistance (R_f), and the charge transfer resistance (R_{ct}), were calculated. The values of R_s and R_{ct} of the MnO$_2$ electrode were much smaller than those of the Mn$_2$O$_3$ electrode, resulting in a much better rate performance for the MnO$_2$ electrode (Fig. 3(c) and Table 1).
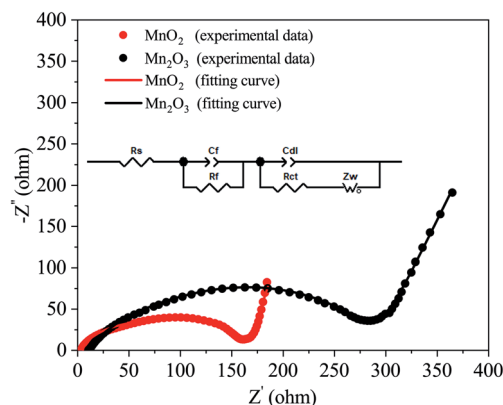

Fig. 4 Nyquist plots of the MnO$_2$ and Mn$_2$O$_3$ electrodes after charging to ~1.9 V vs. Zn^{2+}/Zn.

© 2021 The Author(s). Published by the Royal Society of Chemistry

RSC Adv., 2021, 11, 14408–14414 | 14411

Table 1 EIS fitting results of the MnO$_2$ and Mn$_2$O$_3$ electrodes

	R_s (Ω)	R_f (Ω)	R_{ct} (Ω)
MnO$_2$	3.2	129.5	35.1
Mn$_2$O$_3$	10.3	210.2	72.9

The diffusion barrier of Zn^{2+} in the cathode is also another important factor affecting the electrochemical performance. Since it is challenging to experimentally measure the diffusion barrier of Zn^{2+} in mixed manganese oxides, DFT was used to simulate the diffusion barrier of Zn^{2+} in MnO$_2$ and Mn$_2$O$_3$. The corresponding diffusion pathways are shown in Fig. 5(a) and (b), and the calculated energy profile is displayed in Fig. 5(c) and (d). As shown in Fig. 5(a), the Zn^{2+}-inserted into the α-MnO$_2$ structure was built as a 1 × 1 × 2 supercell with the Zn atom at the hollow site.[26] The calculated energy barrier for the migration of Zn^{2+} in the α-MnO$_2$ structure was 0.497 eV (Fig. 5(c)). For Mn$_2$O$_3$, two different kinds of adjacent interstitial sites were considered for the Zn^{2+} insertion, namely the tetrahedral and octahedral sites. The calculated migration energy barrier for Zn^{2+} in the α-Mn$_2$O$_3$ structure was 1.989 eV (Fig. 5(d)). The migration energy barrier for Zn^{2+} in α-MnO$_2$ was found to be much lower than that in α-Mn$_2$O$_3$, indicating that Zn^{2+} can migrate more easily in α-MnO$_2$. The lower-energy barriers endowed Zn–MnO$_2$ batteries with faster electrochemical kinetics than Zn–Mn$_2$O$_3$ batteries.

In order to obtain the Zn^{2+} diffusion coefficient of the MnO$_2$ and Mn$_2$O$_3$ electrodes, the galvanostatic intermittent titration technique (GITT) was conducted. The GITT was measured at a 0.03 A g^{-1} pulse current for 20 min (τ) and relaxed for 120 min (Fig. 6). The diffusion coefficient of Zn^{2+} ($D_{Zn^{2+}}$, cm^2 s^{-1}) was calculated as:[29]

$$D_{Zn^{2+}} = \frac{4L^2}{\pi\tau}\left(\frac{\Delta E_s}{\Delta E_\tau}\right)^2.$$

where τ is the pulse duration of constant current, and L corresponds to the Zn^{2+} diffusion length, which is equal to the thickness of the electrode. ΔE_s is the voltage change of the termination voltage of two adjacent relaxation steps; ΔE_τ is the potential change during the constant current pulse after eliminating the *IR*-drop.

As calculated, the Zn^{2+} diffusion coefficient of the MnO$_2$ electrode was 3.05×10^{-8} cm^2 s^{-1}, which was higher than that of the Mn$_2$O$_3$ electrode (3.42×10^{-9} cm^2 s^{-1}). The results prove the lower Zn^{2+} diffusion barrier for MnO$_2$ than that of Mn$_2$O$_3$, which is consistent with the computational study.

Based on the above-mentioned results, the MnO$_2$ electrode showed superior electrochemical properties, *i.e.*, higher specific capacity and better rate performance than the Mn$_2$O$_3$ electrode.
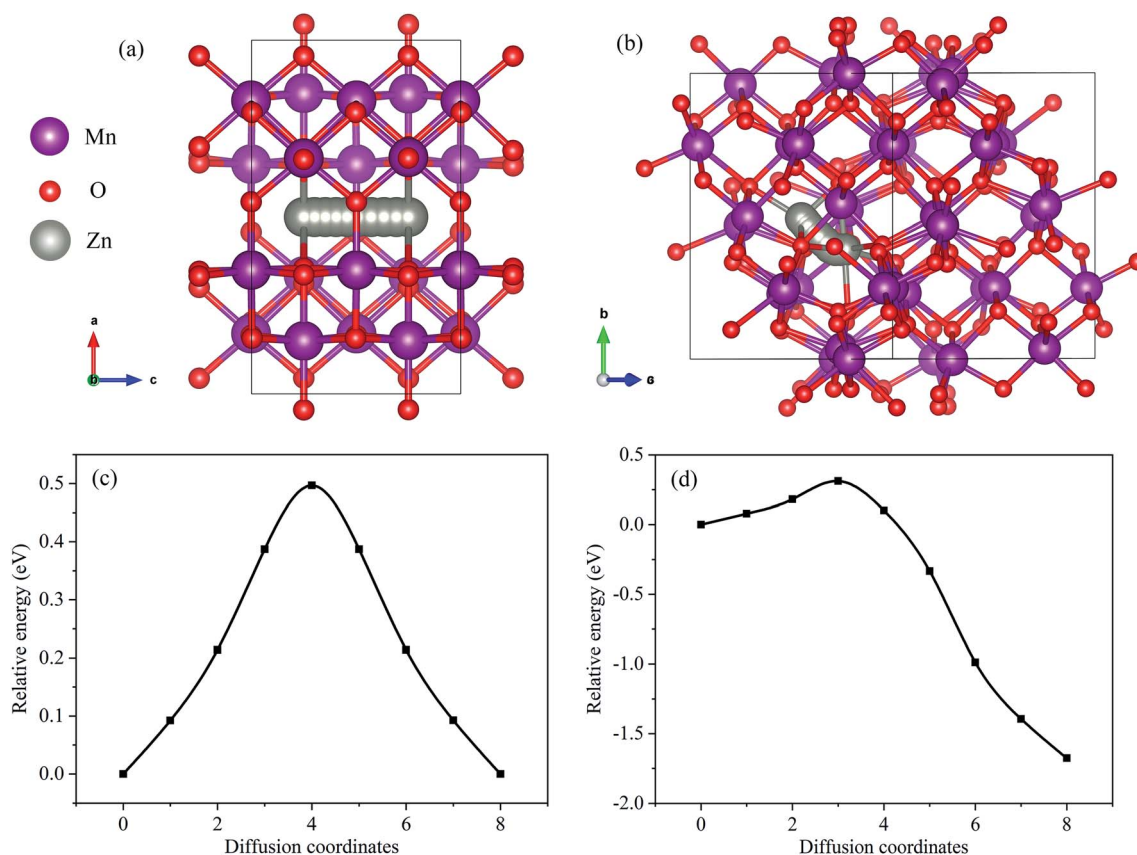

Fig. 5 (a) Zn diffusion pathway in MnO$_2$. (b) Zn diffusion pathway in Mn$_2$O$_3$. (c) The energy landscapes of Zn diffusion in MnO$_2$. (d) The energy landscapes of Zn diffusion in Mn$_2$O$_3$.
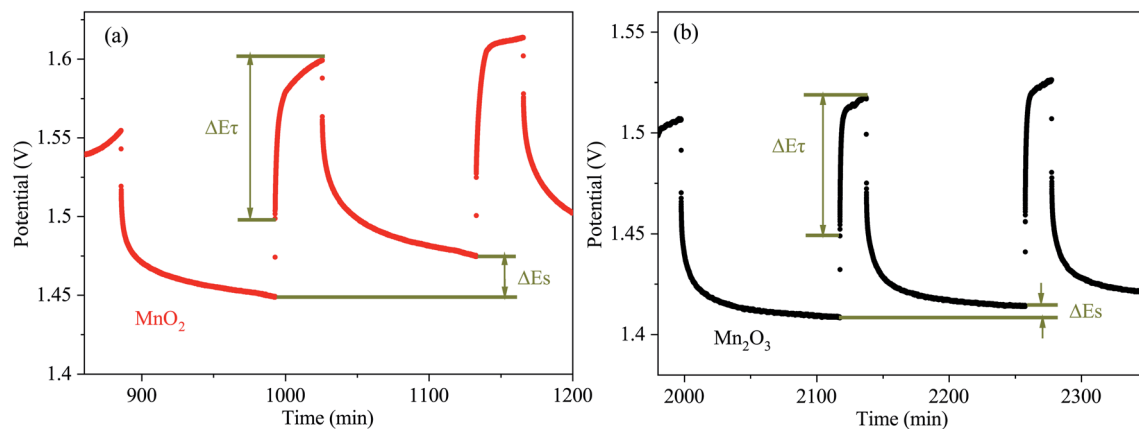
Fig. 6 Scheme for a single titration step of the GITT curves of (a) MnO_2 and (b) Mn_2O_3 electrodes.

The reaction mechanism for MnO_2 has been reported previously that the MnO_2 cathode experiences a consequent H^+ and Zn^{2+} insertion/extraction process during the discharging/charging.[28] In order to reveal the structural reaction mechanism of the Mn_2O_3 electrode, *ex situ* XRD was carried out in numerous discharging/charging states of the Mn_2O_3 electrode, as shown in Fig. S1 (ESI†). The *ex situ* results indicated that the energy storage mechanism of the Mn_2O_3 electrode also involved H^+ and Zn^{2+} insertion/extraction. The superior electrochemical properties of the MnO_2 electrode were ascribed to the following reasons: (i) the α-MnO_2 electrode had a higher electronic conductivity, as evidenced in the decreased charge transfer resistance (Fig. 4), and (ii) the MnO_2 electrode possessed a higher specific surface area (61.9 m^2 g^{-1} for the MnO_2 electrode *vs.* 10.6 m^2 g^{-1} for the Mn_2O_3 electrode), which increased the contact area between the electrode and electrolyte, therefore facilitating the Zn^{2+} insertion process. Moreover, the lower-energy barriers endowed the Zn–MnO_2 batteries with faster electrochemical kinetics. All of these merits contributed to the superior electrochemical performance of the Zn–MnO_2 batteries. It is worth noting that the results also provided an explanation for the lower specific capacity of MnO_x/PPy composites, which contained a higher Mn(III) phase/Mn(IV) phase ratio, as reported in our previous study.[3]

4.   Conclusion

We investigated and compared the electrochemical properties of pure α-MnO_2 and α-Mn_2O_3 as ZIB cathodes *via* a combined experimental and computational study. We demonstrated that the α-MnO_2 electrode possessed a higher specific surface area, higher electronic conductivity, and lower diffusion barrier for Zn^{2+} than that observed in the case of the α-Mn_2O_3 electrode. As a result, the discharging capacity at 0.1 A g^{-1} was higher for the α-MnO_2 electrode (270.4 mA h g^{-1}) than for the α-Mn_2O_3 electrode (188.2 mA h g^{-1}). In addition, α-MnO_2 showed a better rate performance (125.7 mA h g^{-1} at 3 A g^{-1}) than α-Mn_2O_3 (87 mA h g^{-1} at 3 A g^{-1}). This study provides an insight into the electrochemical mechanisms of manganese dioxide-based systems, which can be used to interpret behavior seen in Mn(III)- and Mn(IV)-based phases.

Conflicts of interest

There are no conflicts to declare.

Acknowledgements

References

1 Y. Li, J. Fu, C. Zhong, T. Wu, Z. Chen, W. Hu and J. Lu, *Adv. Energy Mater.*, 2019, **9**, 1802605.

2 P. Yu, Y. Zeng, H. Zhang, M. Yu, Y. Tong and X. Lu, *Small*, 2019, **15**, 1804760.

3 Z. Li, Y. Huang, J. Zhang, S. Jin, S. Zhang and H. Zhou, *Nanoscale*, 2020, **12**, 4150–4158.

4 Y. Huang, Z. Li, S. Jin, S. Zhang, H. Wang, P. Hiralal, G. A. J. Amaratunga and H. Zhou, *Carbon*, 2020, **167**, 431–438.

5 K. Wang, X. Zhang, J. Han, X. Zhang, X. Sun, C. Li and Y. Ma, *ACS Appl. Mater. Interfaces*, 2018, **10**, 24573–24582.

6 M. Alfaruqi, S. Islam, V. Mathew, J. Song, S. Kim, D. Tung and J. Kim, *Appl. Surf. Sci.*, 2017, **404**, 435–442.

7 C. Wang, M. Wang, Z. He, L. Liu and Y. Huang, *ACS Appl. Mater. Interfaces*, 2020, **3**, 1742–1748.

8 D. Wang, L. Wang, G. Liang, H. Li, Z. Liu, Z. Tang and C. Zhi, *ACS Nano*, 2019, **13**, 10643–10652.

9 C. Zhu, G. Fang, J. Zhou, J. Guo, Z. Wang, C. Wang and S. Liang, *J. Mater. Chem. A*, 2018, **6**, 9677–9683.

10 W. Qiu, L. Yu, Y. Ao, Z. Zhang, G. Li and X. Lu, *J. Mater. Chem. A*, 2017, **5**, 14838–14846.

11 N. Palaniyandy, M. Kebede, K. Raju, K. Ozoemena, L. le Roux, M. Mathe and R. Jayaprakasam, *Mater. Chem. Phys.*, 2019, **230**, 258–266.

12 T. Xiong, Y. Zhang, W. S. V. Lee and J. Xue, *Adv. Energy Mater.*, 2020, **10**, 2001769.

13 T. Xiong, Z. G. Yu, H. Wu, Y. Du, Q. Xie, J. Chen, Y.-W. Zhang, S. J. Pennycook, W. S. V. Lee and J. Xue, *Adv. Energy Mater.*, 2019, **9**, 1803815.

14 W. Shi, W. S. V. Lee and J. Xue, *ChemSusChem*, 2021, **14**, 1–26.

15 H. Pan, Y. Shao, P. Yan, Y. Cheng, K. Han, Z. Nie, C. Wang, J. Yang, X. Li, P. Bhattachary, K. T. Mueller and J. Liu, *Nat. Energy*, 2016, **1**, 16039.

16 N. Palaniyandy, M. Kebede, K. Raju, K. Ozoemena, L. le Roux, M. Mathe and R. Jayaprakasam, *Mater. Chem. Phys.*, 2019, **230**, 258–266.

17 B. Wu, G. Zhang, M. Yan, T. Xiong, P. He, L. He and L. Mai, *Small*, 2018, **14**, 1703850.

18 S. Khamsanga, M. T. Nguyen, T. Yonezawa, P. Thamyongkit, R. Pornprasertsuk, P. Pattananuwat, A. Tuantranont, S. Siwamogsatham and S. Kheawhom, *Int. J. Mol. Sci.*, 2020, **21**, 4689.

19 B. Jiang, C. Xu, C. Wu, L. Dong, J. Li and F. Kang, *Electrochim. Acta*, 2017, **229**, 422–438.

20 J. Hao, J. Mou, J. Zhang, L. Dong, W. Liu, C. Xu and F. Kang, *Electrochim. Acta*, 2018, **259**, 170–178.

21 Y. Fu, Q. Wei, G. Zhang, X. Wang, J. Zhang, Y. Hu and S. Sun, *Adv. Energy Mater.*, 2018, **8**, 1801445.

22 B. Lee, H. R. Lee, H. Kim, K. Y. Chung, B. W. Cho and S. H. Oh, *Chem. Commun.*, 2015, **51**, 9265–9268.

23 W. Kohn and L. J. Sham, *Phys. Rev.*, 1965, **140**, A1133–A1138.

24 S. J. Clark, M. D. Segall, C. J. Pickard, P. J. Hasnip, M. I. J. Probert, K. Refson and M. C. Payne, *Z. Kristallogr. - Cryst. Mater.*, 2005, **220**(5/6), 567–570.

25 H. J. Monkhorst and J. D. Pack, *Phys. Rev. B: Solid State*, 1976, **13**, 5188–5192.

26 B. Lee, C. S. Yoon, H. R. Lee, K. Y. Chung, B. W. Cho and S. H. Oh, *Sci. Rep.*, 2014, **4**, 6066.

27 N. Govind, M. Petersen, G. Fitzgerald, D. King-Smith and J. Andzelm, *Comput. Mater. Sci.*, 2003, **28**, 250–258.

28 W. Sun, F. Wang and S. Hou, *J. Am. Chem. Soc.*, 2017, **139**, 9775–9778.

29 D. Zhang, J. Cao, X. Zhang, N. Insin, S. Wang, J. Han and Y. Huang, *Adv. Funct. Mater.*, 2021, 2009412.